Journal of Stress Analysis
Vol. 2, No. 1, Spring – Summer 2017
Bu-Ali Sina University

Coupled Thermoelastic Analysis of Semi-elliptical Crack in Thick-walled Cylinder Considering Green-Lindsay and Green-Naghdi Type II Theories

E. Farahinezhad, A. Nouri*, E. Hosseinian
Aerospace Engineering Department, Shahid Sattari Aeronautical University of Science and Technology, Tehran, Iran.

Article info

Article history:
Received 14 January 2017
Received in revised form
21 April 2017
Accepted 17 July 2017

Keywords:
Green-Naghdi theory
Green-Lindsay theory
Weight function method
Thermal shock
Semi-elliptical crack in cylinder

Abstract

In this paper, the stress intensity factors for semi-elliptical cracks in a homogeneous isotropic cylinder have been determined. Athick-walled cylinder is subjected to a one-dimensional axisymmetric thermal shock on the outer surface according to the classic thermo elasticity (CTE), Green-Lindsay (G-L), and Green-Naghdi (G-N) theories. The effect of temperature-strain coupling and the effect of inertia term in governing equations are considered. The semi-elliptical crack stress intensity factors (SIFs) at the deepest and surface pointsare determined using weight function method. The comparison between the temperature, stress, and SIF obtained from CTE, G-L, and G-N theories shows the different behavior of generalized theories and CTE. By considering relaxation times, prediction of higher temperature and stress values, in contrast to CTE theory, will be resulted. Furthermore, the SIF resulted from generalized theories is significantly higher than CTE theory. The temperature, stress, and maximum SIF obtained for G-N II is higher than G-L theory.

Nomenclature

$\mathbf{b}$	Vector volumetric energy per unit mass	b_r	Radial component of body force
c_1	Dimensionless elastic expansion velocity	$\hat{\mathbf{C}}$	Vector of new material properties in GL theory
$\mathbf{C}$	Fourth order tensor elastic modulus	c_2	Dimensionless shear wave velocity
c_T	Heat wave propagation speed	c_K	GN model damping coefficient
$\mathbf{E}$	Strain tensor	$E1$	Discretization error
K	Stress intensity factor (SIF)	$\mathbf{K}$	Second order tensor thermal conductivity
l	Characteristic length	m_A	Crack weight function
P_i	Internal pressure	$\mathbf{q}$	Heat flux vector
Q	Crack shape factor for the semi-elliptical	q_r	Radial component of heat flux
$R_i,\ R_o$	Inner, outer cylinder radius	σ	Cauchy stress tensor
s	Variable of Laplace transform	S	Entropy per unit volume
$\mathbf{t}$	Thickness	$\mathbf{u}$	Displacement vector
u'	Displacement in in the Laplace	v	Characteristic velocity
T	Absolute temperature	T_d	Characteristic temperature

*Corresponding author: A. Nouri (Assistant Professor)
E-mail address: anouri@ssau.ac.ir
http://dx.doi.org/10.22084/jrstan.2017.12717.1017
ISSN: 2588-2597

T'	Temperature field in the Laplace domain	β	Second order tensor of stress temperature modulus
ε	Coupled thermoelastic parameters	ρ	Mass density
R_s	Internal heat generation per unit volume and time	$l_v(\xi_i R)$, $K_v(\xi_i R)$	Modified type I, II Bessel functions of order v
∇	Gradient operator	$\nabla\cdot$	Divergence operators
∇^2	Laplacian operator		

1. Introduction

Many of the components used in engineering are vulnerable to sudden changes of mechanical and thermal loads. The internal combustion engine cylinders are typical of these structures that are under simultaneous mechanical and thermal loading. In such cases, the rate of load and material property changing can lead to the initiation and growth of cracks. While the classical thermoelasticity theories are suitable for predicting cases that are much greater than the duration required for a single wave front to travel through the thickness of the cylinder, the generalized or coupled thermoelasticity theories are normally applicable to prediction of the transient effects in the early times of the thermoelastic wave propagation. Most of the approaches which were proposed to overcome the inaccurate prediction of the classical theory are based on the general notion of relaxing the heat flux in the classical Fourier heat conduction equation, thereby introducing a non-Fourier effect.

Green and Lindsay [1] modified the Duhamel-Neumann relationships and the entropy relation by introducing two relaxation times that relate the stress and entropy to the temperature rate. Green and Naghdi formulated three models of thermoelasticity for homogeneous and isotropic materials labeled as models I, II, and III. Model I results in thermal diffusion and infinite speed of thermal waves. Model II of Green-Naghdi theory [2] is known as the "thermoelasticity without energy dissipation" and allows for thermal waves to propagate at a finite speed, but without damping. Green-Naghdi type III admits the finite speed of damped thermal wave propagation. Green-Lindsay (GL) and Green-Naghdi (GN) theories are known as the generalized theories, or thermoelasticity theories with secondary sound effect or with finite thermal wave speed. In cases such as Nano-fluids [3], phase changing [4], nuclear reactor technology [5], high-frequency heat therapeutic methods [6] and applying the high heat flux in a short time the secondary sound effects are important. In such cases, the heat field with finite velocity is affected by elastic field and in these conditions the coupled form of governing equations for generalized theories should be used.

Anwar and Sharif calculated temperature, displacement,and thermal stressfields in long hollow cylinders for single [7] and two-layer [8] cases. Laplace transform and displacement potential function were used considering Lord-Shulman theory.

Coupled thermoelastic behavior of multilayer functionally graded cylindrical shell under general mechanical and thermal loading was studied by Fu et al. [9] using Laplace transform. After applying Laplace transform, the time variable is removed from governing equations and ordinary differential equations are simultaneously solved by the use of displacement potential function technique. The effects of heat conduction model, inertia, strain-temperature fields coupling, type of loading, the quality of interface contact, Biot number and the effect of the change in functionally graded material properties on elastic and thermal results were depicted.

Darabseh et al. [10], studied the transient thermo elastic response of a thick-walled cylinder made of FG material under thermal loading regarding Green-Lindsay theory. Material properties varied according to a power law in radial direction. Utilizing galerkin finite element method, the governing equations were solved and the material composition effect on temperature, radial displacement, and thermal stresses was investigated.

Designs of engineering structures are often done in situations where unwanted cracks and defects arise during manufacturing processes or transportation. Under certain conditions these defects and cracks can grow quickly and cause catastrophic failures [11].

Hosseini-Tehrani et al. [12], by using boundary element method and Laplace transform, calculated the dynamic SIF under heat shock by means of G-L theory. The singular behavior of stress in the vicinity of the crack tip was modeled by four-node elements, and SIF for the mode I was calculated according to the displacement fields of nodes. The effect of relaxation time on the strip SIF was also shown. The behavior of coins crack in an infinite thermoelastic solid was studied by Mallik and Kanoria [13] using a unified form of governing equations. The unified form of equations includes CTE theory, Lord-Shulman, and G-N. The Laplace and Henkel transforms were utilized in the solution of the problem and numerical methods were also used for solving integral equations while the temperature, stress and displacement calculated from CTE, Lord-Shulman and G-L theories were presented. Cylinders were one of the widely used components in industrial applications which due to their unique geometric nature, were subjected to periodic loading. Lin and Smith [14] calculated the SIF and fatigue life for a cylinder contain-

ing a half-elliptical crack by using finite element methods. It was also shown that the surface crack turns into a half-elliptical shape after repeated loading. Petroski and Achenbach [15], presented an approximate expression for the displacement of crack surface to calculate the weight function of SIFs for a reference loading. Moreover, the SIF was obtained for a half-plane containing edge cracks, radial cracks from circular hole and also radially cracked rings. Using a weight function method, Shahani and Nabavi extracted a closed form solution for calculating SIF in deepest and surface point so fan axial semi-elliptical crack on a thick-walled cylinder which was under internal pressure and also subjected to steady state [16] and transient [17] thermalloadings. Lee et al. [18], using the boundary integral equation methods, obtained the weight function for longitudinal and hoop cracks. Varfolomeyev and Hodulak [19], derived the weight function for axial and hoop inner surface cracks on an infinitely long cylinder; The proposed weight function was utilized to calculate SIF for uniform tensile loading. More recently, Nazari and Asemi [20] gained the mode I SIF at the deepest and surface point of a half-elliptical crack under hyperbolic thermal loading by means of weight function. The effect of crack aspect ratio on the stress intensity factor of deepest and surface point of the crack was also presented.

Investigation of second sound effect in generalized theories rather than classic theory of thermo elasticity and coupling effectsin generalized theories in prior researches was performed only on temperature and thermal stresses fields and current study investigates the second sound and coupling effects on thermal stress intensity factor. Thermal stress intensity factor is determined in coupled and uncoupled cases and results are compared with classic theory of thermo elasticity. The strain-temperature field coupling and inertia terms are also considered in the governing equations.

2. The Heat Field

In this section, the temperature field in a long cylinder is obtained by the help of CTE, GL, and GN theories. The long hollow cylinder subjected to symmetric boundary conditions and T_0 initial temperature, has an inner radius of r_i and the thickness of t, as shown in Fig. 1. First, the cylindrical shell at ambient temperature is subjected to axisymmetric heat shock on the outer surface at time $t = 0$.

At time $t = 0$, the cylinder is at its initial temperature. At $t = 0^+$, the temperatures of internal and external surfaces will change according to the pre-defined boundary conditions. Using CTE, GL, and GN theories, constitutive equations can be written in terms of unified parameters as follows [21].

$$\nabla \cdot \sigma + \rho \mathbf{b} = \rho \ddot{\mathbf{u}} \tag{1a}$$

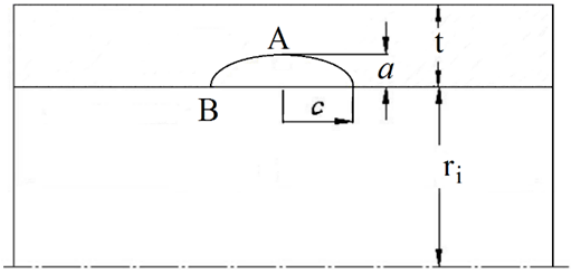

Fig. 1. Axial internal semi-elliptical crack in a cylinder [17].

$$\mathbf{E} = \frac{1}{2}(\nabla \mathbf{u} + (\nabla \mathbf{u})^T) \tag{1b}$$

$$\sigma = \mathbf{C}\mathbf{E} - \beta(T - T_0 + t_1 \dot{T}) \tag{1c}$$

$$\nabla \cdot q = R_s - T_0 \dot{S} \tag{1d}$$

$$S = \left(\frac{\rho c}{T_0}\right)(T + t_2 \dot{T} - T_0) + \beta : \mathbf{E} - \frac{1}{T_0}\hat{\mathbf{C}} \cdot \nabla T \tag{1e}$$

$$\eta \mathbf{q} + t_3 \dot{\mathbf{q}} = -\eta \mathbf{K} \nabla T - t_3 \mathbf{K} \nabla \dot{T} - t_3 \mathbf{K}^* \nabla T - \hat{C} \dot{T} \tag{1f}$$

where equations (1a), (1b), (1c), (1d), (1e), and (1f) are respctively the equation of motion, linear strain-displacement equation, Hooke's Law for linear thermo elastic materials, energy equilibrium equation, the entropy equation, and the equation for the thermal conductivity of GL and GN theories. where ρ is the mass density, σ is the Cauchy's stress tensor, $\mathbf{u}$ is the displacement vector, $\mathbf{b}$ is the body force vector per unit mass, $\mathbf{q}$ is the heat flux vector, T_0 is the reference temperature, T is the absolute temperature, S is entropy per unit volume, R_s is the internal heat source per unit volume per unit time, $\mathbf{E}$ is the strain tensor, β is the second order tensor of stress-temperature moduli, $\mathbf{K}$ is the second order tensor of thermal conductivity, $\hat{\mathbf{C}}$ is the fourth order tensor of elastic moduli, c is the specific heat. Also t_1 and t_2 are the relaxation times and $\hat{\mathbf{C}}$ is a vector of new material constants proposed by Green and Lindsay, and $\mathbf{K}^*$ is the second order tensor of new material constants associated with the GN theory. Also, η and t_3 are terms introduced to consolidate G-L and G-N theories into a unified system of equations. In equations (1), (∇) is the del operator and indicates the gradient of a function. Meanwhile $(\nabla \cdot)$ denotes the divergence operator also $\beta : \mathbf{E}$ In the above equation symbolizes the trace for product of two tensors [21]. To obtain the governing equations, using different theories, the parameter values are assigned as follows:

For CTE theory:

$$\tau = \hat{C} = 0,\ t_1 = t_2 = t_3 = 0,\ \eta = 1$$

For GL theory:

$$\tau = 0,\ \eta = 1, t_3 = t_0 = 0$$

For GN type III theory:

$$\tau = 0,\ \hat{C} = 0,\ \eta = t_1 = t_2 = 0,\ t_3 = 1$$

The governing equations for GN theories type I and II are respectively obtained by approaching $\mathbf{K}^* \to 0$ and $\mathbf{K} \to 0$ in the governing equations resulted from GN type III theory. The energy and equilibrium governing equations based on GL and GN theories for thick-walled cylinders are expressed as follows [22].

$$t_3\kappa^*\nabla^2 T + t_3 k\nabla^2\dot{T} + \eta\frac{k}{t_0}\int_0^t \exp(-(t-\tilde{t})/t_0)(\nabla^2 T)d\tilde{t}$$
$$-\rho c(t_2+t_3)\ddot{T} - \rho c\eta\dot{T} - \rho T_0\beta(\nabla\cdot\dot{\mathbf{u}}) - t_3 T_0\beta(\nabla\cdot\ddot{\mathbf{u}})$$
$$= \eta R_s + t_3\dot{R}_s = 0 \tag{2a}$$

$$\mu\nabla^2 u + (\lambda+\mu)\nabla(\nabla\cdot u) - \beta V(T + t_1\dot{T}) + \rho\mathbf{b} = \rho\ddot{u} \tag{2b}$$

In the above equations, ∇^2 is the Laplacian operator. The thermal conductivity equation for GL and G Ntheories for homogeneous, isotropic materials can be written as follows [21].

$$\eta\mathbf{q} + t_3\dot{\mathbf{q}} = -\eta k\nabla T - t_3 k\nabla\dot{T} - t_3 k^*\nabla T \tag{3}$$

The following dimensionless variables are introduced for simplification.

$$\bar{\mathbf{R}} = \frac{r}{l}$$
$$t' = \frac{v}{l}t$$
$$\bar{u} = \frac{\lambda+2\mu}{l\beta T_d}\mathbf{u}$$
$$\bar{t}_0 = \frac{v}{l}t_0$$
$$\bar{t}_1 = \frac{v}{l}t_1$$
$$\bar{t}_2 = \frac{v}{l}t_2$$
$$\bar{t}_3 = \frac{v}{l}t_3 \tag{4}$$
$$\bar{T} = \frac{T-T_0}{T_d}$$
$$\bar{\sigma} = \frac{\sigma}{\beta T_d}$$
$$\bar{q} = \frac{q}{\rho c v T_d}$$
$$\bar{R}_s = \frac{lR}{\rho c v T_d}$$
$$\bar{\mathbf{b}} = \frac{\beta l T_d}{(\lambda+2\mu)v^2}\mathbf{b}$$

where l, v, and T_d are the characteristic length, velocity, and temperature respectively. For simplification purposes the bar symbol is removed from the variables. Equations (2) and (3) in terms of dimensionless parameters in cylindrical coordinates can be written as follows [22].

$$t_3 c_T^2\left[\frac{\partial^2}{\partial R^2} + \frac{1}{R}\frac{\partial}{\partial R}\right]T + t_3 c_K^2\left[\frac{\partial^2}{\partial R^2} + \frac{1}{R}\frac{\partial}{\partial R}\right]\dot{T}$$
$$+\eta\frac{c_K^2}{t_0}\int_0^t \exp(-(\tau-\tilde{t})/t_0)\left(\left[\frac{\partial^2}{\partial R^2} + \frac{1}{R}\frac{\partial}{\partial R}\right]T\right)d\tilde{t}$$
$$-\varepsilon\left[t_3\left(\frac{\partial}{\partial R} + \frac{1}{R}\right)\ddot{u} + \eta\left(\frac{\partial}{\partial R} + \frac{1}{R}\right)\dot{u}\right] - (t_2+t_3)\ddot{T}$$
$$-\eta\dot{T} + \eta R_s + t_3\dot{R}_s = 0 \tag{5a}$$

$$c_1^2\frac{\partial}{\partial r}\left[\frac{\partial}{\partial R} + \frac{1}{R}\right]u - c_1^2\left(\frac{\partial T}{\partial R} + t_1\frac{\partial\dot{T}}{\partial R}\right) + b_r = \ddot{u} \tag{5b}$$

$$\eta q_r + t_3\dot{q}_r = -(\eta c_k^2 + t_3 c_T^2)\frac{\partial T}{\partial R} - t_3 c_K^2\frac{\partial\dot{T}}{\partial R} \tag{5c}$$

where

$$c_1^2 = \frac{\lambda+2\mu}{\rho v^2}$$
$$c_2^2 = \frac{\mu}{\rho v^2}$$
$$c_T^2 = \frac{\kappa^*}{\rho c v^2} \tag{6}$$
$$c_K^2 = \frac{k}{\rho c l v}$$
$$\varepsilon = \frac{\beta^2 T_0}{\rho c(\lambda+2\mu)}$$

With c_1 representing the dimensionless elastic expansion velocity, c_2 dimensionless shear wave velocity, c_T heat wave propagation speed, c_K GN model damping coefficient and is coupled thermoelastic parameter. Moreover, u is the radial displacement components, b_r theradial component of body force and q_r is the radial component of heat flux. The initial conditions for temperature, displacement, and heat flux are assumed as follows.

$$\begin{cases} u(R,0) = 0 \\ \dot{u}(R,0) = 0 \\ T(R,0) = 0 \\ \dot{T}(R,0) = 0 \\ q(R,0) = 0 \end{cases} \tag{7}$$

Writing the equations (5) in the Laplace domain and regarding the initial conditions expressed in (7)

leads to the following ordinary differential equations in terms of locations.

$$(t_3 + c_T^2 + st_3c_k^2)\left[\frac{\partial^2}{\partial R^2} + \frac{1}{R}\frac{\partial}{\partial R}\right]T' + (\eta + t_3 s)R_s$$

$$-(t_2 + t_3)s^2T' - \eta sT' - \varepsilon[t_3 s^2 + \eta s]\left(\frac{\partial}{\partial R} + \frac{1}{R}\right)u'$$

$$+\eta + \frac{c_k^2}{t_0 s + 1}\left[\frac{\partial^2}{\partial R^2} + \frac{1}{R}\frac{\partial}{\partial R}\right]T' = 0 \quad (8a)$$

$$c_1^2\frac{\partial}{\partial r}\left[\frac{\partial}{\partial R} + \frac{1}{R}\right]u' - c_1^2(1 + t_1 s)\frac{\partial T'}{\partial R} + b_r = s^2u' \quad (8b)$$

$$(\eta + \eta t_0 s + t_3 s)q_r' = -(\eta c_k^2 + t_3 c_T^2 + st_3 c_k^2)\frac{\partial T'}{\partial R} \quad (8c)$$

where s is the standard variable of Laplace transform. u' is obtained by Laplace transformation of u, and T symbolizes the temperature field in the Laplace domain. The displacement potential function is presented as below.

$$u' = \frac{\partial \psi}{\partial R} \quad (9)$$

Equations (8), in the absence of internal heat generation and body forces, can be written in the form shown in equation (10) using the displacement potential function.

$$\beta_1\nabla^2\psi = \beta_2\nabla^2\tilde{\theta} - \tilde{\theta} \quad (10a)$$

$$\beta_3\nabla^2\psi - s^2\psi = \beta_4\tilde{\theta} \quad (10b)$$

$$q_r' = -\beta_5\frac{\partial T'}{\partial R} \quad (10c)$$

where

$$\beta_1 = \frac{\varepsilon[t_3 s^2 + \eta s]}{(t_2 + t_3)s^2 + \eta s}$$

$$\beta_2 = \frac{t_3 c_T^2 + st_3 c_k^2 + \eta\dfrac{c_K^2}{t_0 s + 1}}{(t_2 + t_3)s^2 + \eta s}$$

$$\beta_3 = c_1^2 \quad (11)$$

$$\beta_4 = c_1^2(1 + t_1 s)$$

$$\beta_5 = \frac{\left((\eta c_K^2 + t_3 c_T^2 + st_3 c_K^2)\right)}{(\eta + \eta t_0 + t_3 s)}$$

Removing $\tilde{\theta}$ from equations (10a) and (10b) yields the ordinary differential equations with constant coefficients shown in equation (12).

$$A\nabla^4\psi + B\nabla^2\psi + C\psi = 0 \quad (12)$$

where

$$A = \frac{\beta_3\beta_2}{\beta_4}$$

$$B = -\frac{\beta_2 s^2}{\beta_4} - \frac{\beta_3}{\beta_4} - \beta_1 \quad (13)$$

$$C = \frac{s^2}{\beta_4}$$

The solution to the linear ordinary differential equation (12) in terms of modified Bessel functions can be expressed as below.

$$\psi(R, s) = D_1 I_0(\xi_1 R) + D_2 K_0(\xi_1 R) + D_3 I_0(\xi_2 R) + D_4 K_0(\xi_2 R) \quad (14)$$

The displacement and temperature fields can be respectively determined by substituting the above equation in equations (9) and (10b).

$$u'(R, s) = \varepsilon_1[D_1 I_1(\xi_1 R) - D_2 K_1(\xi_1 R)] + \xi_2[D_3 I_1(\xi_2 R) - D_4 K_1(\xi_2 R)] \quad (15a)$$

$$T'(R, s) = \gamma_1[D_1 I_0(\xi_1 R) + D_2 K_0(\xi_1 R)] + \gamma_2[D_3 I_0(\xi_2 R) + D_4 K_0(\xi_2 R)] \quad (15b)$$

where $I_v(\xi_i R)$ and $K_v(\xi_i R)$ are the modified type I and II Bessel functions of order $v \cdot \xi_i$ can be determined using the constants in equation (13) as below.

$$\varepsilon_{1,2} = \left\{\frac{-B \pm \sqrt{B^2 - 4AC}}{2A}\right\} \quad (16)$$

Coefficients γ_1 and γ_2 can be also expressed as the following form.

$$\gamma_1 = \frac{\beta_3\xi_1^2 - s^2}{\beta_4}$$

$$\gamma_2 = \frac{\beta_3\xi_2^2 - s^2}{\beta_4} \quad (17)$$

Temperature, displacement, and heat flux fields were analytically determined in Laplace domain and unknown coefficients D_i $(i = 1, 2, 3, 4)$ were assigned for the problem based on the assumed boundary conditions. The dimensionless thermal and mechanical boundary conditions in inner and outer surfaces of the cylinder are as follows:

$$T'(R_i, s) = 0$$

$$T'(1, s) = 1/s$$

$$u'(R_i, s) = 0 \quad (18)$$

$$u'(1, s) = 0$$

After determining the unknown coefficients by the help of boundary conditions (18), the temperature field can be mapped to time domain using numerical inverse Laplace transform depicted in the Appendix.
The material that was used (in ref. 21 and current study) is aluminum and consequently all results belong to this material. Dimensionless values were used for thermal parameters instead of introducing ordinary values that have dimension. Thermal and mechanical properties of aluminum are represented in Table 1.

Table 1
Aluminum thermal and mechanical properties.

Property	α	c	ρ	E	v
Value	23e-6	0.896	2707	70	0.346

For mapping the results into time-domain, the following values for relevant dimensionless parameters were used [22].

$$\begin{cases} c_1 = 1 \\ C_T = 0.535 \\ \epsilon = 0.02 \end{cases} \tag{19}$$

To extract the results of the GL theory, the following values for the dimensionless parameters were selected according to what is stated in reference [22].

$$\begin{cases} t_1 = 4 \\ t_2 = 4 \\ C_K = 1 \end{cases} \tag{20}$$

According to the above values, the thermal wave speed for GL theory is expressed as follows.

$$\frac{C_K}{\sqrt{t_2}} = 0.5 \tag{21}$$

For GN type II theory, the results are obtained substituting the following values.

$$t_3 = 4 \tag{22a}$$

$$C_T = 0.5 \tag{22b}$$

$$C_K = 0 \tag{22c}$$

In GN theory the heat wave speed can be extracted using equation (22-2).

3. The Hoop Stress Field

In this section, the hoop stress field of the cylinder can be determined analytically in the Laplace domain using the temperature field. The effects of inertia term and also the effect of strain-temperature fields coupling are considered in the governing equations. The hoop stress in a cylinder in terms of temperature distribution is proposed in reference [21] which is presented in equation (23)

$$\sigma_\Phi = \frac{E\alpha}{1-v}\left[\frac{1}{r_0^2 - r_i^2}\left(1+\frac{r_i^2}{r^2}\right)\int_{r_i}^{r_o} rTdr + \frac{1}{r^2}\int_{r_i}^{r} rTdr - T\right] \tag{23}$$

The hoop stress suggested in the above equation can be dimensionless by the help of equation (24)

$$S'_\Phi = \frac{\sigma_\Phi(1-v)}{E\alpha T_d} \tag{24}$$

By substituting the equation (23) into equation (24), the dimensionless hoop stress can be obtained as below.

$$S'_\Phi(r,s) = \frac{1}{1-R_i^2}\left(1+\frac{R_i^2}{R^2}\right)\int_{R_i}^{1} RT'dR + \frac{1}{R^2}\int_{R_i}^{R} RT'dR - T' \tag{25}$$

After substitution of the non-dimensional temperature field equation into equation (25), the dimensionless hoop stress of the cylinder can be obtained in the Laplace domain as follows

$$\begin{aligned} S'_\Phi(R,s) = {} & \frac{1}{D_1(1-R_i^2)}\left(1+\frac{R_i^2}{R^2}\right)\Big[A_5 I_1(D_1) + A_6 K_1(D_1) \\ & - R_i(A_5 I_1(D_1 R_i) + A_6 K_1(D_1 R_i))\Big] + \frac{1}{R^2 D_1}\Big[R(A_5 \\ & + I_1(D_1 R) + A_6 K_1(D_1 R)) - R_i(A_5 I_1(D_1 R_i) \\ & + A_6 K_1(D_1 R_i))\Big] - A_5 I_0(D_1 R) + A_6 K_0(D_1 R) \\ & + \frac{1}{D_2(1-R_i^2)}\left(1+\frac{R_i^2}{R^2}\right)\Big\{A_7 I_1(D_2) + A_8 K_1(D_2) \\ & - R_i(A_7 I_1(D_2 R_i) + A_8 K_1(D_2 R_i))\Big\} + \frac{1}{R^2 D_2}\Big\{R(A_7 I_1(D_2 R)) \\ & + A_8 K_1(D_2 R) - R_i(A_7 I_1(D_2 R_i) + A_8 K_1(D_2 R_i))\Big\} \\ & - A_7 I_0(D_2 R) + A_8 K_0(D_2 R) \end{aligned} \tag{26}$$

After determining the hoop stress field in the Laplace domain, the hoop stress field in the thick-walled cylinder can be mapped into time domain using numerical methods.

4. SIF Determination of Semi-elliptical Crack

4.1. The Weight Function Method

Most of the existing methods for calculating SIF demand a separate analysis of geometry and loading, i.e. changing the geometry or load necessitates the repetition of the analysis. The weight function method provided by Bueckner [23] and Rice [24], is considered as an efficient method for determining the SIF which makes the calculation much easier. Weight function splits up the loading and geometry effects on calculating SIF; so that if the weight function, $m(r,a)$, for a crack-containing body with known geometry is available, the SIF can be calculated for any arbitrary loading. Integrating the product of stress distribution within a geometry in absence of crack and weight function on the assumed crack surface yields the SIF.

Hitherto, weight function has been determined for different crack geometries. First, the weight function based on the crack surface openings corresponding to the reference loadings has been stated [25] which requires the analytical solution of the problem on its own. To solve the above problem, various methods are proposed such as the crack surface opening approximate function [26] and approximate weight function, which is normally applicable to a particular geometry. In the case of one-dimensional radial loading, the weight function for the cracks deepest point (point A in Fig. 1) is proposed as follows [17].

$$m_A(r,a)=\sqrt{\frac{2}{\pi}}\sqrt{\frac{1}{r_i+a-r}}+M_{A1}\sqrt{\frac{2}{\pi a}}+M_{A2}\sqrt{\frac{2}{\pi}}\frac{1}{a}\sqrt{r_i+a-r}+M_{A3}\sqrt{\frac{2}{\pi a^3}}(r_i+a-r) \tag{27}$$

where $r=r_i+a$ expresses the position of crack tip. The weight function for the surface points of semi-elliptical crack (point B in Fig. 1) is proposed in the form of equation (28) [17].

$$m_B(r,a)=\sqrt{\frac{4}{\pi}}\sqrt{\frac{1}{r-r_i}}+M_{B1}\sqrt{\frac{4}{\pi a}}+M_{B2}\sqrt{\frac{4}{\pi a}}\frac{1}{a}\sqrt{r-r_i}+M_{B3}\sqrt{\frac{4}{\pi a^3}}(r-r_i) \tag{28}$$

The shape factor for the semi-elliptical crack is described inequation (29)

$$Q=1+1.464\left(\frac{a}{c}\right)^{1.65} \tag{29}$$

For the deepest point of a semi-elliptical crack, the coefficients M_{Ai} $(i=1,2,3)$, are in the form shown by equation (30)

$$M_{A1}=\frac{2\pi}{\sqrt{2Q}}(Y_0-3Y_1)+\frac{24}{5}$$
$$M_{A2}=3 \tag{30}$$
$$M_{A3}=\frac{6\pi}{\sqrt{2Q}}(2Y_1-Y_0)-\frac{8}{5}$$

where

$$Y_0=B_0+B_1\left(\frac{a}{t_c}\right)+B_2\left(\frac{a}{t_c}\right)^2+B_3\left(\frac{a}{t_c}\right)^4$$
$$Y_1=A_0+A_1\left(\frac{a}{t_c}\right)+A_2\left(\frac{a}{t_c}\right)^2+A_3\left(\frac{a}{t_c}\right)^4 \tag{31}$$

In [17], the coefficients A_i and B_i are introduced as exponential functions of (a/c). For semi-elliptical crack's surface point sconstants, M_{Bi} $(i=1,2,3)$, are as depictedin equation (32).

$$M_{B1}=\frac{3\pi}{\sqrt{Q}}(2F_1-5F_0)-8$$
$$M_{B2}=\frac{15\pi}{\sqrt{Q}}(3F_1-F_0)+15 \tag{32}$$
$$M_{B1}=\frac{3\pi}{\sqrt{Q}}(3F_0-10F_1)-8$$

In which correction factors for geometry can be obtained by the use of curve fitting as in equation (33)

$$F_0=\left[C_0+C_1\left(\frac{a}{t_c}\right)+C_2\left(\frac{a}{t_c}\right)^2+C_3\left(\frac{a}{t_c}\right)^4\right]\left(\frac{a}{c}\right)$$
$$F_1=\left[D_0+D_1\left(\frac{a}{t_c}\right)+D_2\left(\frac{a}{t_c}\right)^2+D_3\left(\frac{a}{t_c}\right)^4\right]\left(\frac{a}{c}\right) \tag{33}$$

For the radius ratio of $R_o/(R_i=1.25)$ the coefficients C_i and D_i are introduced as polynomial functions in [16].

4.2. SIF Determination

Given the stress is a continuous function of r and weight function, the SIF can be determined. SIF for cracks deepest point can be determined using the weight function for cracksdeepest crack's deepest point and the expression in equation (34).

$$K_A=\int_0^a m_A(r,\alpha)\sigma_\varphi(r)dr \tag{34}$$

The SIF for the surface points of a semi-elliptical crack on theinternal surface can be computed using equation (35).

$$K_B=\int_0^a m_B(r,\alpha)\sigma_\varphi(r)dr \tag{35}$$

Fitting second order polynomial curves on the hoop stress before and after the discontinuity was used,

which led to more stable results in comparison to the numerical integration method [20]. If the position of discontinuity is assumed to be ρ, the hoop stress distribution can be divided into two parts, before and after the discontinuity, to make the curve fitting more accurate.

$$S'_{h1} = A_1R^2 + B_1R + C_1, \quad R_i \le R \le R_i + \rho \quad (36a)$$

$$S'_{h2} = A_2R^2 + B_2R + C_2, \quad R_i + \rho \le R \le R_0 \quad (36b)$$

5. Results and Discussion

In this section, the temperature, hoop stress, and stress intensity factors calculated for a long cylinder with semi-elliptical crack on the inner surface are presented in the time domain. For validation purposes, the temperature distribution calculated from GL and GN theories are compared with the results published in reference [22]. In the mentioned reference, inner and outer radii of the cylinder are $R_i = 1$ and $R_o = 2$ respectively. Figs. 2 and 3 are concluded from the boundary conditions shown in equation (37) which is stated in reference [22]. The comparison of results is performed for four times confirming the sufficient accuracy of the obtained results.

$$q'_r(R_i, s) = \frac{10000}{s(s+100)^2}$$
$$u'(R_i, s) = 0,\ T'(R_0, s) = 0,\ S'_r(R_0, s) = 0 \quad (37)$$

According to Figs. 2 and 3, the two GL and GN theories confirm the finite speed of heat wave. At any moment, according to equation (37), the applied heat flux on the inner surface of the cylinder causes the temperature change only in points that are between the inner surface and the heat wave front. Moreover, the discontinuity in temperature-heat wave speed graphs are in well correspondence with equations (22) and (38-b).

By applying the thermal shock to the cylinder, the energy loss is small in the initial times and can be neglected. Therefore the GN type II theory is suitable for analyzing the thermal shock at initial times. Comparison of Figs. 2 and 3 indicates that GL theory, in contrast to the GN theory, does not predict any sudden discontinuity in the temperature graph which originates from the thermal conductivity equation used in the theory. In GL theory, the Fourier thermal conductivity equation is utilized and heat flux is dependent on the temperature gradient. Moreover, the heat flux rate is not included in thermal conductivity equation of GL theory. While in the thermal conductivity equation of GN type II theory, the rate of heat flux is not dependent on temperature gradient. The thermal conductivity equations of the two theories can be expressed as follows.

$$(q_r)_{GL} = -c_K^2 \frac{\partial T}{\partial R} \quad (38a)$$

$$(\dot{q}_r)_{GN} = -c_T^2 \frac{\partial T}{\partial R} \quad (38b)$$

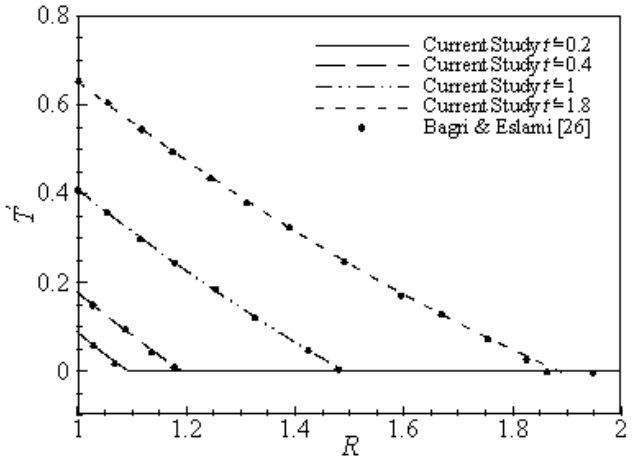

Fig. 2. GL temperature distribution.

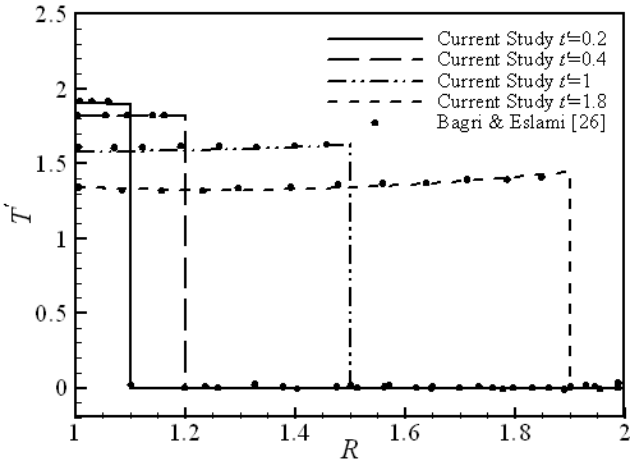

Fig. 3. Green-Naghdi temperature distribution.

Using the boundary conditions in (37), the dimensionless hoop stress graph is plotted based on G-L theory. The results are also compared with those presented in [22] at three different times as shown in Fig. 4. According to the figure, in a like manner to the temperature distribution, the stress wave also propagates with a finite speed within the cylinder.

In Fig. 5, the non-dimensional hoop stress resulted from GN theory and the boundary conditions (37) is compared with the results published in reference [22] at three different times. In Figs. 4 and 5, propagation of thermal and elastic waves in the radial direction of cylinder is shown. As shown in the figure, at time $t' = 0.2$, the first discontinuity occurs at the position of $R = 1.1$ which originates from the heat wave. The second discontinuity in hoop stress occurs at $R = 1.2$ which, according to the unit speed of elastic wave and equation (20a), is due to the elastic wave. According

to Figs. 4 and 5, the hoop stress resulted from the current study are in complete agreement with those presented in reference [22], confirming the accuracy of the attained results.

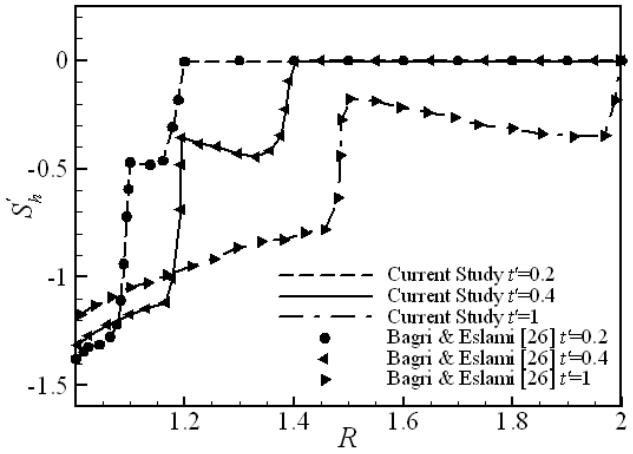

Fig. 4. GL hoop stress distribution.

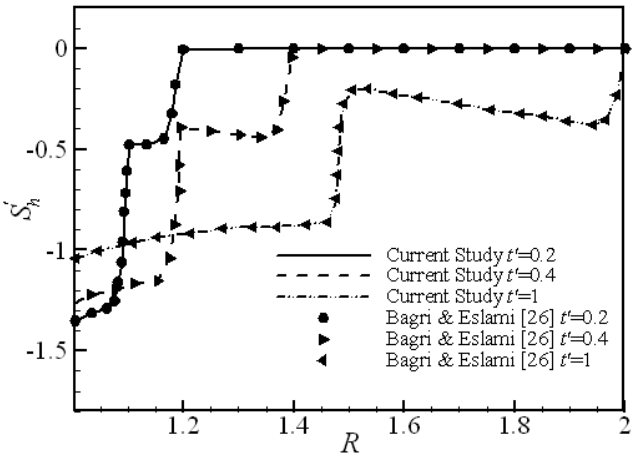

Fig. 5. G-N hoop stress distribution.

With respect to the numerical inversion of Laplace transform method presented by [27], an initial guess for CON ($= v.\tau$) equal to 5 should be considered, and then suggested procedure in [27] optimizes the Laplace transform parameter (s). In other words, Laplace transform parameter determinates by minimizing truncation and discretization errors. "s" is an imaginary number and equals to $V + i$W. According to this reference, after this optimization process real part of "s" will be in the $1 < V < 18$ range. Another parameter that affects optimized "s" is singularities of the function that is mapped numerically from Laplace domain to time space so that V should be greater than real part of all mentioned functions's singularities.

The magnitude of V for Figs. 4 and 5 are represented in Table 2. To verify the accuracy of results, the SIF for the deepest and surface points of semi-elliptical crack are compared by those obtained from the weight function method proposed in [20] in Tables 3 and 4.

Table 2
The material properties of concrete specimens.

R	Fig. 4	Fig. 5
1.025	16.12146	14.75145
1.05	11.41847	10.96439
1.075	15.10377	14.55243
1.1	12.19548	13.87284
1.125	14.97539	14.90122
1.15	16.07051	14.30029
1.175	13.20717	12.90162
1.2	13.27567	13.55871
1.225	17.56589	14.83696
1.25	13.30484	12.81183
1.275	17.03927	16.08232
1.3	15.62033	15.84149
1.325	14.79691	13.99193
1.35	14.58224	13.92567
1.375	13.21901	12.66302
1.4	12.81773	12.0516
1.425	13.31697	11.24905
1.45	7.829444	9.043247
1.475	6.930915	6.549061
1.5	8.056337	8.492867
1.525	7.635103	6.806276
1.55	9.791462	7.764695
1.575	8.805568	8.18932
1.6	10.20513	9.313489
1.625	10.14451	10.40014
1.65	11.40883	10.57845
1.675	13.38324	11.83841
1.7	11.46781	10.41729
1.725	13.65477	11.16833
1.75	10.32084	10.73057
1.775	7.058097	8.093935
1.8	9.213539	9.834115
1.825	8.196829	8.131849
1.85	9.112848	9.233337
1.875	8.741133	8.924204
1.9	12.56741	10.78702
1.925	7.589578	8.188326
1.95	10.56639	10.14988
1.975	8.13007	7.872307

The results are obtained by disregarding the effect of strain-temperature fields coupling and by using the steady state condition for two GL and GN theories, which should be consistent with the results of Fourier's law. The results presented in Tables 3 and 4 are achieved by assuming an initial internal temperature of $T(R_i, 0) = -100$, an internal pressure of $P_i = 10$MPa in a cylinder with a radius ratio of $R_o(R_i = 1.25)$. The SIF values in Tables 1 and 2 can beturned into dimensionless quantities using the following equation.

$$K_N = \frac{K}{P_i\sqrt{\pi a}} \tag{39}$$

The closeness of the results presented in the current research to those reported in [19], confirms the efficacy

of the utilized weight function method for calculating precise SIF values. Temperature and hoop stress fields obtained from employing the boundary conditions expressed in equation (18) were mapped to the space domain using numerical methods. In this section, based on the regarded boundary conditions, heat and stress waves are always traveling from the outer wall to the inner wall of the cylinder. Moreover, the stress intensity factor was determined by fitting second order polynomial curves on terms of dimensionless hoop stress and using the weight function methods.

Table 3
Deepest points SIFs.

[19]	GL	GN	a/t	a/c
20.81	20.79	20.8	0.2	0.2
18.80	18.80	18.81	0.4	
17.71	17.70	17.71	0.6	
16.40	16.40	16.41	0.8	
18.98	18.98	18.99	0.2	1
13.53	13.53	13.53	0.4	
8.13	8.12	8.13	0.6	
2.79	2.79	2.8	0.8	

Table 4
Surface points SIFs.

[19]	GL	GN	a/t	a/c
14.12	14.12	14.13	0.2	0.2
15.55	15.54	15.55	0.4	
17.91	17.90	17.92	0.6	
20.78	20.78	20.80	0.8	
26.01	26.01	26.02	0.2	1
25.08	25.08	25.08	0.4	
24.55	24.54	24.55	0.6	
24.30	24.28	24.30	0.8	

Fig. 6 demonstrates the effect of coupled thermoelastic parameter on the temperature distribution obtained by GL and GN theories by radius. The finite speed of heat wave is clearly visible on the graph; and the heat wave speed obtained by GL and GN theories is consistent with the value obtained from (21) and (22b). According to the GL theory, temperature graph at time $t' = 0.5$, after the heat wave has reached the inner wall and returned to the outer wall, changed in all cylinder locations; while in GN theory, temperature distribution at time $t' = 0.2$, only points are located between outer wall of cylinder and thermal wave front, has changed. According to the figure, it can be deduced that in the uncoupled state, which is plotted for thermoelastic parameter of $\varepsilon = 0$, the speed of the heat wave is larger than that of the coupled state, which is plotted for $\varepsilon = 0.02$. This issue originates from the effect of strain-temperature fields coupling which reduces the heat wave speed.

The non-dimensional hoop stress distribution resulted from GL theory at time $t' = 0.5$ and GN theory at time $t' = 0.2$ are shown in Fig. 7. In the uncoupled and coupled states the thermoelastic parameters are assumed as $\varepsilon = 0$ and $\varepsilon = 0.02$ respectively. As it is evident in the figure, the stress wave speed shown in the graph is in good agreement with Fig. 6; discontinuities occur at the same point in both graphs. Furthermore, in the uncoupled state the stress wave propagates through the cylinder with a higher speed in comparison to the coupled state. Unlike temperature distribution predicted by the GN theory presented in Fig. 6, where the temperature has only changed in points located between the inner wall and heat wave front, the hoop stress distribution throughout the whole cylinder is subjected to change as soon as the cylinder temperature changes. This issue originates from the zero mechanical loading on the cylinder and also the nonexistence of internal and external pressure; and the area under the hoop stress graph will be zero at a certain time.

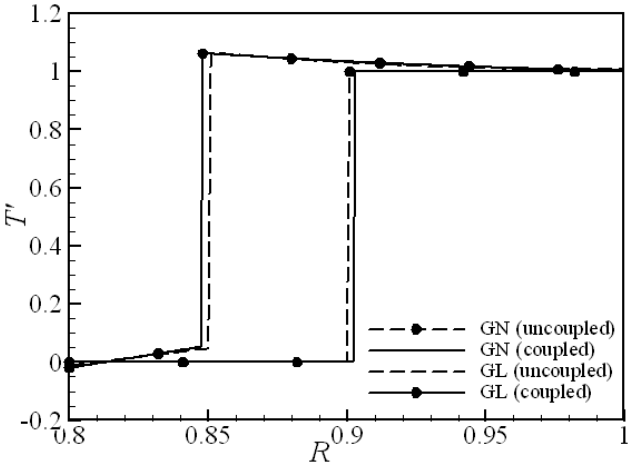

Fig. 6. Coupling thermo elastic parameter effect on GL ($t' = 0.5$) and GN ($t' = 0.2$) temperature distributions.

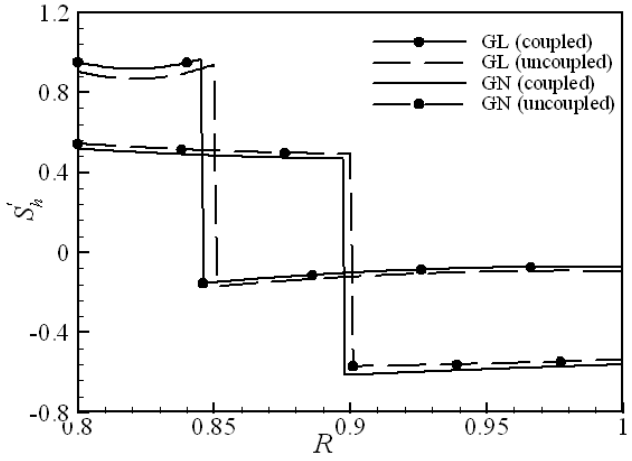

Fig. 7. Coupling thermo elastic parameter effect on GL ($t' = 0.5$) and GN ($t' = 0.2$) hoop stress distributions.

Table 3 compares the temperature and hoop stress calculated by CTE, GL, and GN theories at time

$t' = 0.3$. At this time, heeding the finite speed of heat wave obtained by the generalized theories, the temperature barely changes for points located at $R = 0.85$, which is between the outer wall and the heat wave front. However, the results of temperature obtained by CTE theory, which is presented for the same moment, demonstrates the infinite speed of the heat wave; this is due to the fact that the temperature changes at all points of the cylinder. Additionally, at the mentioned time, the temperature distribution obtained by CTE theory at position $R = 0.85$ is 25% of the value predicted by GL and 23% of the value computed by GN theory.

In Figs. 8 and 9, time variation of thermal hoop stress is represented for coupled G-L and G-N theories respectively. According to the results, as wave front propagates toward internal surface of cylinder, the maximum hoop stress increases.

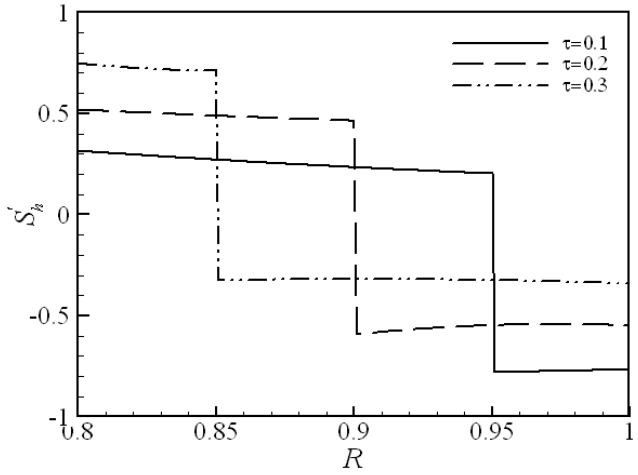

Fig. 8. Coupled Green-Lindsay hoop stress time variation.

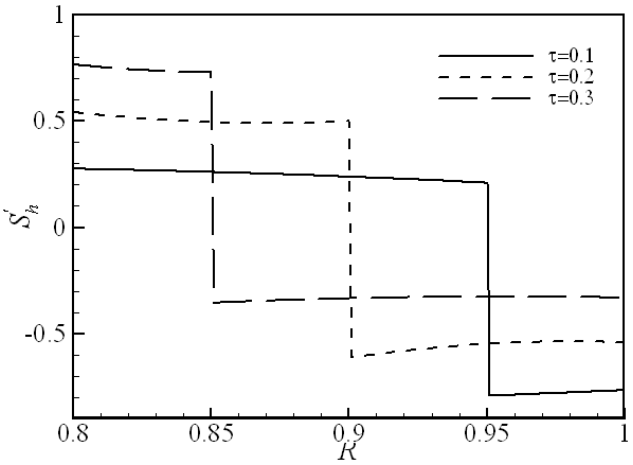

Fig. 9. Coupled Green-Naghdi hoop stress time variation.

Table 5 also shows that the hoop stress has non-zero value for points where the temperature remains unchanged. Comparing stress results between the generalized and CTE theories in the vicinity of the internal surface of cylinder shows significant difference between results of these theories, so that CTE theory underestimates hoop stress in this region and defects and cracks could initiate and propagate due to the higher thermal hoop stress. The stress value predicted by generalized theories is about 4 times the amount anticipated by CTE theory.

Fig. 10 exhibits the effect of coupled thermo elastic parameter on the SIF calculated by generalized theories at the deepest point of a semi-elliptical crack. The SIF calculated by GL theory at the time $t' = 0.5$ and that obtained by G N theory at time $t' = 0.2$ are plotted. According to the figure, the SIF starts to increase from zero value until it reaches its peak, which is for a crack whose tip is in the location of stress wave; then, according to compressive nature of loop stress and also the singularity of weight function, the SIF decreases until it reaches a steady value.

Table 5
Temperature and hoop stress of CTE, GL,and GN theories at $t' = 0.3$.

	CTE		GL		GN	
Dimensionless radius	Temperature	Hopp stress	Temperature	Hopp stress	Temperature	Hopp stress
0.82	0.110	0.181	0	0.725	0	0.742
0.84	0.218	0.131	0	0.713	0	0.730
0.86	0.323	0.082	1.077	-0.322	1.116	-0.349
0.88	0.426	0.036	1.056	-0.320	1.089	-0.340
0.9	0.527	-0.007	1.039	-0.318	1.066	-0.333
0.92	0.626	-0.050	1.025	-0.319	1.046	-0.328
0.94	0.722	-0.091	1.015	-0.322	1.031	-0.325
0.96	0.817	-0.129	1.008	-0.326	1.019	-0.324
0.98	0.909	-0.166	1.005	-0.332	1.011	-0.326

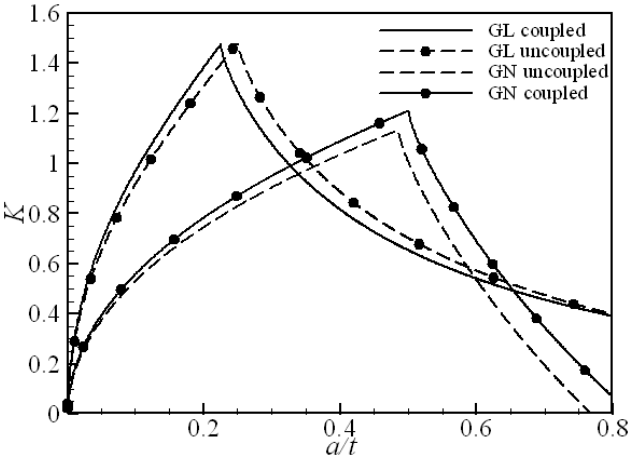

Fig. 10. The effect of coupling thermoelastic parameter on GL ($t' = 0.5$) and GN ($t' = 0.2$) SIFs.

Heeding the coupled diagrams shown in Fig. 10 it is evident that when the SIF curve discontinuity approaches to the inner surface (the short crack length), the predicted maximum SIF becomes larger; in other words, the maximum SIF through the crack length is larger for short cracks compared with deep cracks (which are close to the outer surface of cylinder). This result indicates the vulnerability of the inner surface of cylinder to creation and growth of cracks which is the result of the assumed boundary conditions.
The SIF presented in Figs. 10 and 11 and also Table 6, is dimensionless using the variable shown in equation (40).

$$K = \frac{(1-v)}{E\alpha T_d\sqrt{r_0}} K_I \tag{40}$$

Fig. 11 shows the effect of coupled thermoelastic parameter on the SIF calculated by GL and GN theories for the surface points of semi-elliptical crack.It can be seen that the SIF obtained by GL (since it is closer to the inner surface of cylinder in comparison to GN theory) is larger than that of GN theory. It was also observed that in uncoupled case the SIFat the crack's surface points is larger than the coupled state. Moreover, the SIF at the crack's surface points increases by lengthening the relative crack length, thus it reaches its maximum at the relative length of $a/t = 0.8$.

Table 6 compares the SIFs obtained by generalized theories and CTE for the deepest and surface points of a semi-elliptical crack at time $t' = 0.3$. It can be deduced that SIF calculated by the generalized theories is 1.9 times, at the deepest point of the crack, and 1.5 times, at the surface points of crack, larger than CTE.

According to the data presented in Table 6, prediction of larger quantities by generalized theories based on equation (33) leads to greater area under curve of stress diagram at any moment and thus greater SIF.

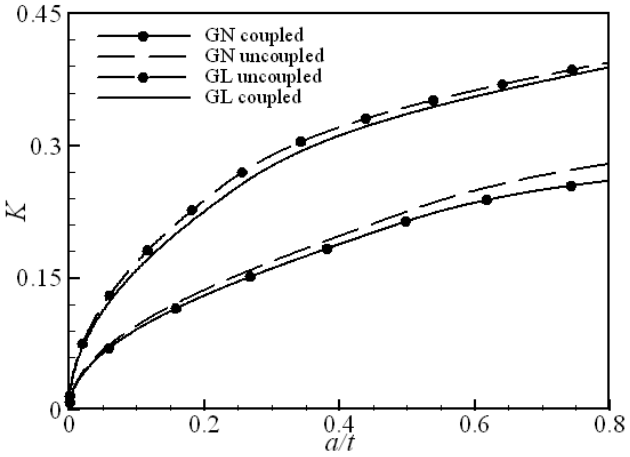

Fig. 11. The effect of coupling thermoelastic parameter on GL ($t' = 0.5$) and GN ($t' = 0.2$) surface point SIFs of semi-elliptical crack.

Fig. 12 and Fig. 13 represent the time variation of G-L and G-N deepest point SIFs as a function of relative crack depth respectively. As represented, stress wave is generated from cylinder outer surface and it propagates toward the inner surface of cylinder. It is observed that at a certain time, the stress intensity factor at the deepest point decreases as the relative depth increases. An important fact in this problem is the effect of applied thermal shock on the stress intensity factors.

Table 6
Deepest and surface points SIFs based on CTE, GL and GN theories at $t' = 0.3$.

Cracks relative length	Deepest	Surface	Deepest	Surface	Deepest	Surface
0.1	0.456	0.085	0.767	0.132	0.784	0.135
0.2	0.559	0.116	1.079	0.187	1.104	0.192
0.3	0.579	0.138	0.891	0.229	0.903	0.235
0.4	0.5497	0.156	0.535	0.254	0.531	0.260
0.5	0.481	0.170	0.292	0.270	0.280	0.275
0.6	0.385	0.182	0.104	0.280	0.089	0.286
0.7	0.266	0.192	-0.051	0.288	-0.066	0.293
0.8	0.127	0.200	-0.185	0.293	-0.199	0.298

According to the figures, two different behaviors may be recognized. The first part corresponds to the cracks with small a/t (i.e., relative crack depths less than about 0.2-0.3), in which the maximum stress intensity factor at the deepest point occurs at small instants of time and as the time elapses the stress intensity factor becomes significantly smaller. The second part relates to the deep cracks (i.e., relative depths greater than about 0.2-0.3), where the maximum stress intensity factor occurs in the steady state. In other words, cracks with small depths are much more critical while subjected to thermal shock and crack growth may occur under cooling condition at small times.

Furthermore, as a wave propagates toward inner surface and time elapses, maximum SIF increases, which refers to its stress distribution and force balance equation. In other words, as the wave propagates toward the internal surface, magnitude of stress in neighborhood of internal surface of cylinder increases to recompense the force balance condition.

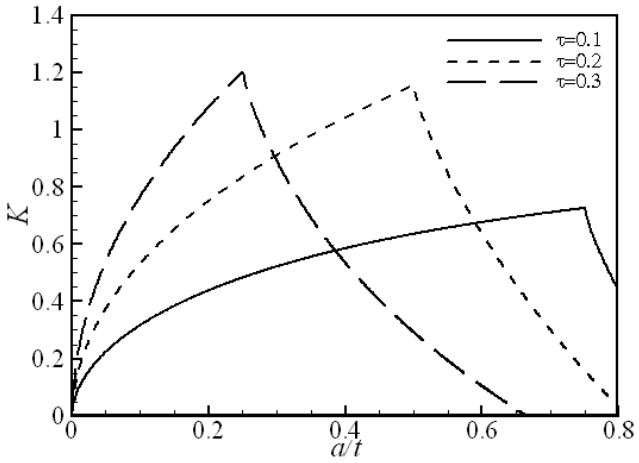

Fig. 12. Time variation of coupled G-L deepest point SIFs.

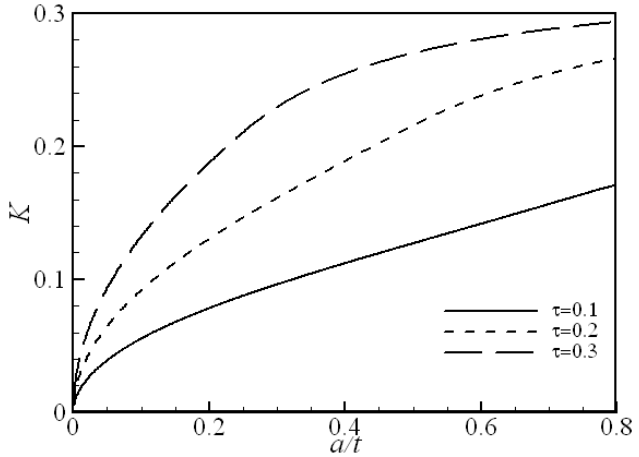

Fig. 13. Time variation of coupled G-L surface points SIFs.

Fig. 13 and Fig. 14 depict time variation of G-L and G-N surface points SIFs as a function of relative crack depth respectively. It is observed that stress intensity factor has different behaviors at deepest point and surface points where refers to the different weight function for these points. As represented in the mentioned figures, it is seen that at a certain time, the stress intensity factor at the corner points increases with the increase of crack relative depth.

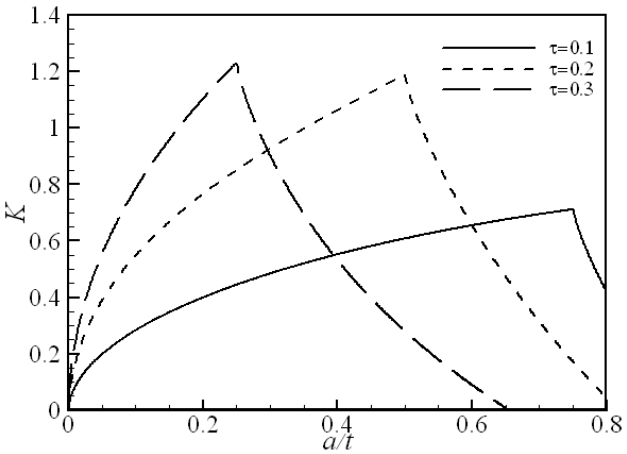

Fig. 14. Time variation of coupled G-N deepest point SIFs.

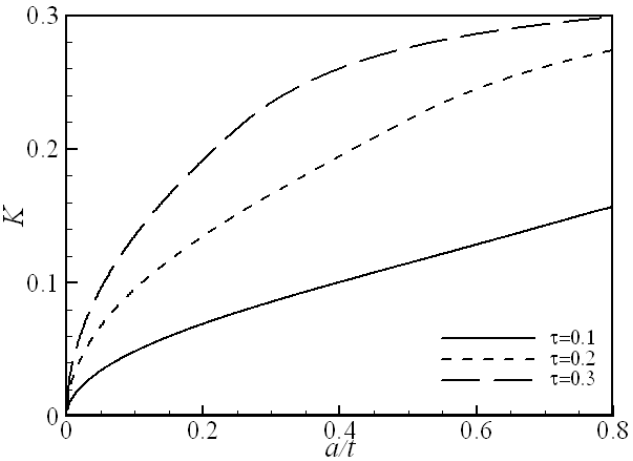

Fig. 15. Time variation of coupled G-N surface points SIFs.

Comparing the maximum SIF value at a certain time in Fig. 12 (Fig. 13) with corresponding time in Fig. 14 (Fig. 15), yields that G-N theory predicted higher maximum stress intensity factor rather than G-L theory, which refers to neglecting energy dissipation in its governing equations. Figs. 16 and 17 show the effect of aspect ratio a/c on the SIF at the deepest and surface points of a semi-elliptical crack. It can be concluded that reduction of crack aspect ratio causes the maximum increase in SIF at the deepest and surface points of a semi-elliptical crack.

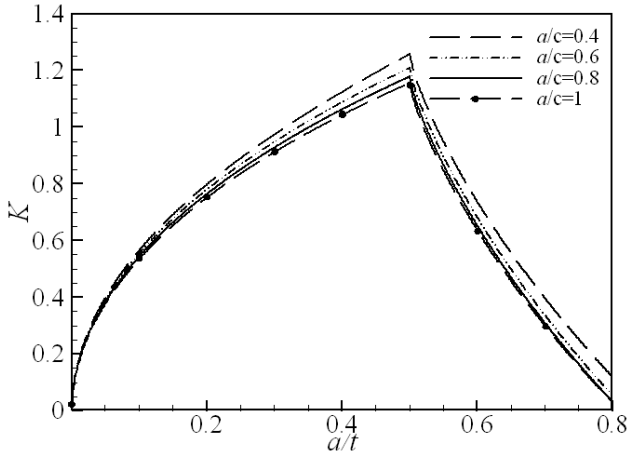

Fig. 16. The effect of crack aspect ratio on deepest point SIFs based on GL theory.

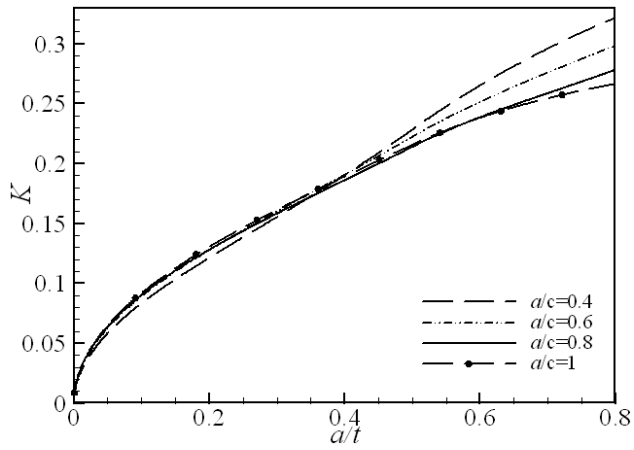

Fig. 17. The effect of crack aspect ratio on surface points SIFs based on GL theory.

According to Fig. 14, at $a/c = 1$ the semi-elliptical crack deform into a half circle; in other words, the SIF at the deepest and surface points of a semi-elliptical crack decreases when the crack approaches the semi-circle shape. Comparing among thermal SIFs at $a/t = 0.5$ for different crack aspect ratios shows that, the crack with $a/c = 0.4$ has 9% higher thermal SIF than crack with $a/c = 1$. Similarly, as shown in Fig. 17, for $a/t = 0.8$ the SIF is 20% larger than the semi-circular crack at the diagram discontinuity point.

6. Conclusions

In this paper, the SIF at the deepest and surface points of a semi-elliptical crack existing on the inner surface of a thick-walled cylinder, which is subjected to hyperbolic thermal shock according to GL and GN theories, was obtained. The summary of results is as follows:

1. In cases where the heat flux boundary condition is implemented on the cylinder, GL and GN theories predict completely different temperature distributions.
2. Considering the coupling effect in the governing equations of generalized theories leads to a reduction in speed of heat and stress waves in comparison to uncoupled case.
3. Considering the relaxation times in the governing equations of generalized theories would lead to prediction of larger maximum values for temperature, stress and thus SIF, when compared with CTE theory.
4. SIF value through the crack length is larger for short cracks. This shows that the inner surface of the cylinder is more susceptible to crack initiation and growth in comparison to the outer surface.
5. Atinitial times after applying the thermal shock, the SIF predicted by the generalized theories at the deepest point of shallow cracks is muchlarger than CTE theory. The maximum SIF at the crack's deepest point occurs when the stress wave front reaches the crack tip.
6. SIF at the cracks deepest point increases at first, then gradually decreases to a steady value.
7. For shallow cracks, the aspect ratio does not exert much influence on its behavior. But with the passage of time and the deepening of the crack, the effect of aspect ratio on SIF increases.
8. The SIF anticipated by the generalized theories for the crack's surface points is always larger than that of CTE theory. This issue can be of drastic importance when predicting the unstable crack growth. Longitudinal growth of crack reduces the diametric aspect ratio and thus increases the SIF at the crack's deepest point.
9. GL and GN theories predict similar results for temperature, stress, and SIF when thermal boundary condition of type I is implemented. The minor difference in their results arises from disregarding the lossin GN theory.

According to different results of generalized theories and CTE theory for a crack under thermal loading, choosing the appropriate theory for thermoelastic analysis and design of structures is of particular importance.

Appendix

The inverse Laplace transform of function $\tilde{f}(s)$ is defined by equation (41)

$$f(t) = \mathcal{L}^{-1}\{\tilde{f}(s)\} = \frac{1}{2\pi i}\int_{v-i\infty}^{v+i\infty} \tilde{f}(s)e^{st}ds \qquad (41)$$

where, $i=\sqrt{-1}$ and $s=v+iw$. v is an arbitrary real value which is greater than the real part of all singular points of function $\tilde{f}(s)$. Equation (41) can also be expressed as below.

$$f(t)=\frac{e^{vt}}{\pi}\int_0^{\infty}[\mathrm{Re}\{\tilde{f}(s)\}\cos wt-\mathrm{Im}\{\tilde{f}(s)\}\sin wt]dw \quad (42)$$

An approximate equation is proposed for calculating the Laplace transform of function $f(t)$ by using Fourier expansion of $g(t)=e^{-vt}f(t)$ in the interval $[0,2\pi]$.

$$f(t)=\frac{e^{vt}}{\pi}\Bigg[-\frac{1}{2}\mathrm{Re}\{\tilde{f}(s)\}+\sum_{n=0}^{\infty}\mathrm{Re}\left\{\tilde{f}\left(v+i\frac{n\pi}{\tau}\right)\right\}\cos\frac{n\pi}{\tau}t$$

$$-\sum_{n=0}^{\infty}\mathrm{Im}\left\{\tilde{f}\left(v+i\frac{n\pi}{\tau}\right)\right\}\sin\frac{n\pi}{\tau}t\Bigg]-E1(v,t,\tau) \quad (43)$$

$E1\ (v,t,\tau)$ is the discretization error which can be is expressed as

$$E1(v,t,\tau)=\sum_{n=1}^{\infty}e^{-2nv\tau}f(2\pi\tau+t) \quad (44)$$

The discretization error can be reduced by choosing larger values for v. Approximating infinite series in (43) by N terms, causes another error in computation known as accumulation error.

$$f(t)=\frac{e^{vt}}{\tau}\Bigg[-\frac{1}{2}\{\tilde{f}(s)\}+\sum_{n=0}^{N}\mathrm{Re}\left\{\tilde{f}\left(v+i\frac{n\pi}{\tau}\right)\right\}\cos\frac{n\pi}{\tau}t$$

$$-\sum_{n=0}^{\infty}\mathrm{Im}\left\{\tilde{f}\left(v+i\frac{n\pi}{\tau}\right)\right\}\sin\frac{n\pi}{\tau}t\Bigg]-E1(v,t,\tau)$$

$$+E2(N,v,t,\tau) \quad (45)$$

The accumulation error is expressed as follows:

$$E2(N,v,t,\tau)=\frac{e^{vt}}{\tau}\Bigg(\sum_{n=N+1}^{\infty}\mathrm{Re}\left\{\tilde{f}\left(v+i\frac{n\pi}{\tau}\right)\right\}\cos\frac{n\pi}{\tau}t$$

$$-\sum_{n=N+1}^{\infty}\mathrm{Im}\left\{\tilde{f}\left(v+i\frac{n\pi}{\tau}\right)\right\}\sin\frac{n\pi}{\tau}t\Bigg) \quad (46)$$

In [27] a method of correction is proposed to reduce discretization and accumulation error. According to equation (44), discretization error can be reduced by setting a larger value for $v\tau$. On the other hand, extremely large values for $v\tau$ may cause the divergence of accumulation error described in equation (45). The method proposed in [27] leads to a reduction of discretization error without any increase in the accumulation error. Moreover, an optimal estimation of v, by the use of the constants N and τ, is resulted. In this method, the optimum value for v is achieved by minimizing the summation of discretization and accumulation errors.

References

[1] A.E. Green, K.A. Lindsay, Thermoelasticity, J. Elast., 2(1) (1972) 1-7.

[2] A.E. Green, P.M. Naghdi, A re-examination of the basic postulate of thermomechanics, Proceedings of the Royal Society of London, 432(1885) (1991) 171-194.

[3] J.J. Vadasz, S. Govender, P. Vadasz, Heat transfer enhancement in nano-fluids suspensions: possible mechanisms and explanations, Int. J. Heat. Mass. Trans., 48(13) (2005) 2673-2683.

[4] A. Miranville, R. Quintanilla, A generalization of the Caginalp phase - field system based on the Cattaneo law, Nonlinear. Anal. Theor., 71(5) (2009) 2278-2290.

[5] G.E. Spinosa-Paredes, E.G. Espinosa-Martinez, Fuel rod model based on non-Fourier heat conduction equation, Ann. Nucl. Energy, 36(5) (2009) 680-693.

[6] J.A. Lopez Molina, M.J. Rivera, M. Trujillo, E.J. Berjano, Effect of the thermal wave in radiofrequency ablation modelling: an analytical study, Phys. Med. Biol., 53(5) (2008) 1447-1462.

[7] H.H. Sherief, M.N. Anwar, A problem in generalized thermoelasticity for an infinitely long annular cylinder, Int. J. Eng. Sci., 26(3) (1988) 301-306.

[8] H.H. Sherief, M.N. Anwar, A problem in generalized thermoelasticity for an infinitely long annular cylinder composed of two different materials, Actamechanica, 80(1-2) (1989) 137-149.

[9] J.W. Fu, Z.T. Chen, L.F. Qian, Coupled thermoelastic analysis of a multi-layered hollow cylinder based on the C-T theory and its application on functionally graded materials, Compos. Struct., 131(1) (2015) 139-150.

[10] T. Darabseh, N. Yilmaz, M. Bataineh, Transient thermoelasticity analysis of functionally gradedthick hollow cylinder based on GreenLindsay model, Int. J. Mech. Mater. Des., 8 (2012) 247-255.

[11] R. Simpson, J. Trevelyan, Evaluation of J1 and J2 integrals for curved cracks using an enriched boundary element method, Eng. Fract. Mech., 78(4) (2011) 623-637.

[12] P. Hosseini-Tehrani, M.R. Eslami, S. Azari, Analysis of thermoelastic crack problems using Green-Lindsay theory, J. Thermal. Stress., 29(4) (2006) 317-330.

[13] S.H. Mallik, M. Kanoria, A unified generalized thermoelasticity formulation: application to penny-shaped crack analysis, J. Thermal. Stress., 32(9) (2009) 943-965.

[14] X.B. Lin, R.A. Smith, Numerical analysis of fatigue growth of external surface cracks in pressurized cylinders, Int. J. Pres. Ves. Pip., 71(3) (1997) 293-300.

[15] H.J. Petroski, J.D. Achenbach, Computation of the weight function from a stress intensity factor, Eng. Fract. Mech., 27(6) (1987) 697-715.

[16] A.R. Shahani, S. M. Nabavi, Closed-form stress intensity factors for a semi-elliptical crack in a thick-walled cylinder under thermal stress, Int. J. Fatigue., 29(8) (2006) 926-933.

[17] S.M. Nabavi, A.R. Shahani, Thermal stress intensity factors for a cracked cylinder under transient thermal loading, Int. J. Pres. Ves. Pip., 86 (2009) 153-163.

[18] H.Y. Lee, Y.W. Kim, I. Yun, Stress intensity factor solution for radial and circumferential cracks in hollow cylinders using indirect boundary integral, Int. J. Pres. Ves. Pip., 69(1) (1996) 45-52.

[19] I.V. Varfolomeyev, L. Hodulak, Improved weight functions for infinitely long axial and circumferential cracks in a cylinder, Int. J. Pres. Ves. Pip., 70(2) (1197) 103-109.

[20] M.B. Nazari, O. Asemi, Stress intensity factor for a longitudinal semi-elliptical crack in a thick-walled cylinder under hyperbolic thermal loading, Modares Mechanical Engineering, 14(6) (2015) 143-151.

[21] R.B. Hetnarski, M.R. Eslami, Thermal Stresses: Advanced Theory and Applications, New York, Springer, (2009) 255-256.

[22] A. Bagri, M.R. Eslami,A unified generalized thermoelasticity; solution for cylinders and spheres, Int. J. Mech. Sci., 49(12) (2007) 13251335.

[23] H.F. Bueckner, principle for the computation of stress intensity factors, Zeitchrift fur Angewandte Math. Mech., 50(9) (1970) 129-146.

[24] J.R. Rice, Remarks on elastic crack-tip stress fields, Int. J. Solids. Struct., 8(6) (1972) 751-758.

[25] S.M. Nabavi, A.R. Shahani, Thermal stress intensity factors for a cracked cylinder under transient thermal loading, Int. J. Pres. Ves. Pip., 86(2) (2009) 153-163.

[26] K.Y. Lee, K.B. Sim, Thermal shock stress intensity factor by bueckners weight function method, Eng. Fract. Mech., 37(4) (1190) 779-804.

[27] G. Honig, U. Hirdes, A method for the numerical inversion of Laplace transform, J. Comput. Appl. Math., 10(1) (1984) 113-132.